

Multiparameter estimation using multi-echo spoiled gradient echo with variable flip angles and multicontrast compressed sensing

Daiki Tamada¹ | Tetsuya Wakayama² | Hiroshi Onishi¹ | Utaroh Motosugi¹

¹Department of Radiology, University of Yamanashi, Yamanashi, Japan

²GE Healthcare Japan, Tokyo, Japan

Correspondence

Daiki Tamada, Department of Radiology,
University of Yamanashi, 1110
Shimokato, Chuo-shi, Yamanashi-ken
409-3898, Yamanashi, Japan.
Email: dtamada@yamanashi.ac.jp

Purpose: To develop multiparameter mapping including T_1 , R_2^* , and proton density fat fraction with a single breath-hold to evaluate liver disease and liver function.

Methods: A 6-echo spoiled gradient-echo sequence with dual flip angles was used to acquire a 12-set MRI volume data set. To shorten the scan time, undersampling and multicontrast compressed-sensing reconstruction were used. The scan time was 18 seconds. R_2^* and proton density fat fraction mapping were achieved by using the iterative least-squares method. T_1 mapping was estimated using driven equilibrium single-pulse observation of T_1 . Quantitative values were validated by performing phantom and volunteer studies.

Results: Statistical analysis showed that the quantitative values measured using the proposed methods agreed with those measured using conventional methods. T_1 values of water proton measured by the proposed method in phantom and volunteer studies were in good agreement with those by MRS.

Conclusion: The results showed that accurate quantitative mapping of T_1 , R_2^* , and proton density fat fraction with a single breath-hold was achieved using our approach.

KEYWORDS

imaging, magnetic resonance imaging, multi-echo spoiled gradient echo phantoms

1 | INTRODUCTION

Magnetic resonance imaging enables noninvasive and quantitative analysis of liver disease. Liver biopsy is the gold-standard for the diagnosis of liver fibrosis and fatty liver disease, although there are several limitations such as invasiveness and sampling error as a result of small volume of the biopsy specimen, which represents only approximately 1/50 000 of the whole liver.¹ Previous studies revealed that sampling error in liver biopsy as a result of the heterogeneous distribution of the disease may lead to misclassification of steatohepatitis² or poor diagnostic

performance in intermediate fibrosis.³ Various MRI-based methods have been proposed for the noninvasive assessment of liver disease. Several studies have reported the utility of diffusion-weighted MRI for the evaluation of liver fibrosis, which uses the characteristic diffusion restriction by structural features of fibrosis (such as collagen fibers).⁴ However, DWI has some challenges such as low image quality and artifacts caused by cardiac motion. Magnetic resonance elastography (MRE), which measures the viscoelastic properties of soft tissues, is also used for assessment of fibrosis⁵ and enables a noninvasive staging of liver fibrosis.⁶ However, measurement difficulty in

patients with hepatic iron-overload⁷ and low availability due to high cost are the limitations of magnetic resonance elastography.

T_1 quantitative mapping is emerging as a potentially useful quantitative biomarker in the liver.^{8–10} Previous reports have suggested that the concentration of gadoxetate disodium (Gd-EOB-DTPA, EOB Primovist, Bayer Healthcare, Berlin, Germany) taken up into the liver is associated with liver function and fibrosis,^{8,9} and signal intensities on T_1 -weighted images were originally used for the estimation of liver function/fibrosis after Gd-EOB-DTPA administration.^{11,12} However, recent papers report that T_1 mapping is a promising approach to accurately estimate liver function using uptake of Gd-EOB-DTPA.¹³ In addition, native T_1 of the liver is supposed to be prolonged by liver fibrosis, which can be useful for MR-based liver fibrosis staging without a contrast agent or elastography.¹⁰

Many studies have reported successful T_1 mapping of the liver using shortened MOLLI,¹⁰ the turboFLASH,¹¹ multi-slice EPI¹³, or multi-echo spoiled gradient echo (SPGR).¹⁴ Although these approaches enable fast and reliable mapping, acquiring the whole-liver T_1 mapping with a single breath-hold has not been attempted.

To estimate fibrotic changes in the liver by T_1 measurement, bias effect as a result of fat and iron accumulation needs to be considered. In a fatty liver, the excessive triglyceride in liver cells shortens the liver T_1 as a result of the short T_1 and off-resonance characteristics of fat.¹² Liu et al proposed the chemical shift-encoded MRI (CSE-MRI) with the variable flip angle (VFA) approach to remove the bias by measuring the T_1 of water and fat.¹⁴ Iron accumulation also leads to T_1 -shortening. Iron-based bias can be corrected by obtaining a T_2 or a T_2^* map of the liver, as T_2 and T_2^* are associated with the amount of iron accumulation in the liver.¹⁵ In fact, Hoad et al proposed T_1 mapping with a T_2^* cut-off to avoid a T_1 bias effect caused by iron accumulation.¹³ Therefore, T_1 mapping, together with proton density fat fraction (PDFF) and T_2^* mapping, could offer accurate native T_1 data of water protons in the liver, which might be useful to estimate liver fibrosis without contrast agents or additional devices like a vibrator (which is needed for MR elastography).

In this study, we proposed a 3D multiparameter mapping method (VFA method), including T_1 , R_2^* and PDFF, with a single breath-hold, using the multi-echo SPGR sequence with a VFA. To remove the bias to T_1 measurement due to the presence of fat in a voxel, a CSE-MRI-based method was used for water-fat separation.¹⁶ T_1 mapping was performed based on the driven equilibrium single-pulse observation of T_1 (DESPOT-1)¹⁷ using the separated water signal. In addition, R_2^* mapping was performed using the least-squares estimation with a multiple fat spectral peak model for the evaluation of iron accumulation.^{16,18} To shorten the scan

time, compressed sensing (CS) with a total variation regularization approach was used.^{19,20} The sparsity of multicontrast MR images was used for CS reconstruction. T_1 , PDFF, and R_2^* mappings were achieved with single breath-hold imaging. Phantom and volunteer studies were performed to demonstrate and validate the method. The derived quantitative maps showed that fast and reliable results were achieved using the VFA method.

2 | THEORY

The signal acquired with the VFA multi-echo SPGR sequence reflects T_2^* , off-resonance, and T_1 of the voxel. Assuming the multiple spectral peak model of fat, the signal decay using multi-echo sequence is defined as

$$S(t) = \left(\rho_w + \rho_f \sum_{m=1}^M \alpha_m \cdot e^{j2\pi f_m t} \right) \cdot e^{j2\pi \psi t}, \quad (1)$$

where ρ_w and ρ_f represent the proton density of water and fat, respectively; α_m ($\sum_{m=1}^M \alpha_m = 1$) and f_m are the linear relative amplitude and off-resonance frequency for the m th fat peak, respectively; and ψ is the complex field map¹⁸ proposed by Yu et al. The proton density for each fat peak can be expressed as $\rho_f \times \alpha_m$. As shown in Equation 2, ψ is introduced to represent off-resonance frequency ψ_0 and R_2^* effect, expressed as

$$\psi = \psi_0 + j \frac{R_2^*}{2\pi}. \quad (2)$$

The acquired signal of water and fat depends on the flip angles (FAs). Therefore, the signal acquired with multi-echo and VFA can be defined as

$$S_n(t) = \left(\rho_{w(n)} + \rho_{f(n)} \sum_{m=1}^M \alpha_m \cdot e^{j2\pi f_m t} \right) \cdot e^{j2\pi \psi t} \quad (3)$$

where $\rho_{w(n)}$ and $\rho_{f(n)}$ are the signal magnitude of water and fat for the n th FA, respectively.

2.1 | Water-fat separation using the CSE-MRI method

To avoid the bias to T_1 measurement caused by the presence of fat, water-fat separation was achieved using the CSE-MRI method. In the CSE-MRI method, the separation can be achieved using 2 or more MR images with different TEs, which reflect the off-resonance of the fat components. In this study, we used the CSE-MRI approach proposed by Yu et al.¹⁸

In matrix representation, Equation 3 can be expressed as

$$S_n = D A \rho_n, \quad (4)$$

where

$$D = \begin{bmatrix} e^{j2\pi\psi t} & 0 & \dots & 0 \\ 0 & e^{j2\pi\psi t} & & \vdots \\ \vdots & & \ddots & 0 \\ 0 & \dots & 0 & e^{j2\pi\psi t} \end{bmatrix}$$

$$A = \begin{bmatrix} 1 & \sum_{m=1}^M \alpha_m \cdot e^{j2\pi f_m t} \\ 1 & \sum_{m=1}^M \alpha_m \cdot e^{j2\pi f_m t} \\ \vdots & \vdots \\ 1 & \sum_{m=1}^M \alpha_m \cdot e^{j2\pi f_m t} \end{bmatrix} \quad (5)$$

$$\rho_n = \begin{bmatrix} \rho_{w(n)} \\ \rho_{f(n)} \end{bmatrix}$$

ψ can be calculated by using the T_2^* -IDEAL algorithm, which is the iterative least-squares estimation approach.^{16,18} The proton density is then obtained using the following equation:

$$\rho_n = (A^* A)^{-1} A^* \cdot D^* \cdot S_n. \quad (6)$$

2.2 | ESPOT-1 with the water component

T_1 mapping of the water components using the SPGR sequence and linear regression can be achieved using DESPOT-1¹⁷ and separated water signal. T_1 mapping is calculated from 2 or more images acquired using VFA SPGR sequences. The signal equation for the SPGR can be expressed as

$$S_{SPGR(n)} = \frac{M_0(1-E_1)\sin\theta_n}{1-E_1\cos\theta_n}. \quad (7)$$

where $E_1 = e^{-\frac{TR}{T_1}}$; M_0 is a factor proportional to the equilibrium longitudinal magnetization; and θ is the FA. Here, it is clear that $\rho_{w(n)}$ derived in Equation 6 is proportional to S_{SPGR} of the water component. Then, Equation 7 can be rewritten as

$$\frac{\rho_{w(n)}}{\sin\theta_n} = \frac{\rho_{w(n)}}{\tan\theta_n} E_1 + C(1-E_1), \quad (8)$$

where C is the constant coefficient. It can be seen from this equation that E_1 can be determined as the slope m of the linear regression for $\left(\frac{\rho_{w(n)}}{\tan\theta_n}, \frac{\rho_{w(n)}}{\sin\theta_n}\right)$ using the least-squares method. Finally, the T_1 of the water component is obtained as

$$T_1 = -\frac{TR}{\ln(m)}. \quad (9)$$

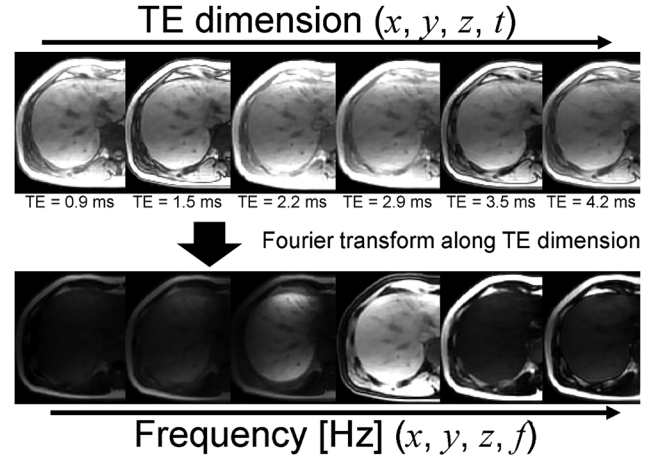


FIGURE 1 Fourier transform of the images acquired with chemical shift-encoded MRI (CSE-MRI) along the TE dimension gives high sparsity. The signal is decomposed in the frequency domain based on the off-resonance frequency of the components

T_1 of fat can also be calculated in the same way using the separated fat signal derived as Equation 6, if fat signal is sufficiently high for the calculation. In the case of low fat fraction, T_1 of fat can be inaccurate using the DESPOT-1. For the stability of the mapping, the regularization method using the assumption of T_1 in the liver will minimize the problem.¹⁴ However, such instability causes little effect on T_1 mapping of water in this study, as it is derived from only separated water signal.

2.3 | Sparse sampling and reconstruction with total variation

The CS reconstruction^{19,20} with multicontrast MR images was used to achieve efficient reconstruction. Compressed sensing reduces scan time by using incoherence sampling and sparsity of the signal. In this study, the total variation was applied to images in the Fourier domain (x, y, z , and f), along with TE dimension for L1 regularization, as shown in Figure 1. This approach leads to high sparsity of the signal, because the signal oscillates along the TE as a result of the off-resonance of water and fat. The reconstruction with multicontrast images using the TV operator can be achieved by solving the following equation:

$$X = \underset{x}{\operatorname{argmin}} \frac{1}{2} \sum_{s=1}^M \|Ax_s - y_s\|^2 + \lambda \| \mathcal{F}_{TE} X \|_{TV}, \quad (10)$$

where $X = [x_1, x_2, \dots, x_s, \dots, x_M]$ is the set of MR images to be reconstructed; x_s and y_s comprise the s th contrast image and acquired k-space data set, respectively; A is the observation matrix; $\| \cdot \|_{TV}$ is the TV operator; and \mathcal{F}_{TE} is the Fourier transform along the TE dimension. The TV operator is defined as

$$\| \mathcal{F}_{TE} X \|_{TV} = \sum_i^N \sqrt{\left(\nabla_1 (\mathcal{F}_{TE} X) \right)_i^2 + \left(\nabla_2 (\mathcal{F}_{TE} X) \right)_i^2 + \left(\nabla_3 (\mathcal{F}_{TE} X) \right)_i^2}, \quad (11)$$

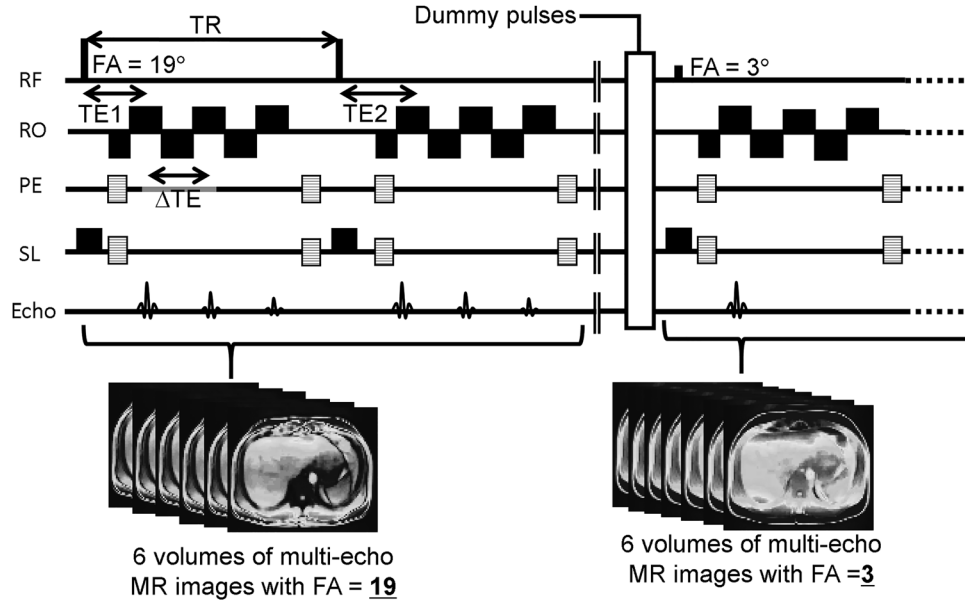


FIGURE 2 Variable flip angle (FA) and multi-echo 6-echo spoiled gradient-echo (SPGR) sequence used in this study. The set dummy pulses were used to maintain the steady state of the SPGR magnetization. RO, readout; PE, phase encode; SL, slice

where N is the number of the voxel; and ∇_1 , ∇_2 , and ∇_3 are the finite-difference operators along the first, second, and third coordinates, such as readout, phase encode, and slice direction. The matrix A is expressed as

$$Ax = PFTSx, \quad (12)$$

where S is the sensitivity map of receiver; T is the spatial phase variation; F is the Fourier transform; and P is the undersampling operator.

3 | METHODS

3.1 | Pulse sequence design

A set of images was acquired using the SPGR sequence with multi-echo, multishot, and VFA on a clinical 3T MRI scanner (Discovery MR750, GE Healthcare, Waukesha, WI). Six echoes were measured using the 3-echo and 2-shot acquisition scheme, as shown in Figure 2. The 3 echoes were separated (ΔTE) by 0.5 to 0.9 ms depending on the FOV, receiver bandwidth, and TR. Each shot had different TEs (TE1, TE3, TE5 in shot 1 and TE2, TE4, TE6 in shot 2), resulting in 6 volume images with echo trains evenly separated. Two sets of 6-volume images were acquired with 2 FAs, which was set as 19° and 3° in this study (see next paragraph). Between the acquisitions of the 2 image sets, a series of dummy pulses, which consisted of 50 RF pulses without readout and phase encoding, was inserted to achieve a steady state of magnetization. Trajectories for undersampling were generated according to a Gaussian distribution to achieve incoherent sampling. Center region (20×16) of k-

space was used for the estimation of a sensitivity map, which was calculated using the ESPIRiT algorithm.²¹

3.2 | Optimization for FA

The FAs used for the T_1 mapping were optimized according to Deoni's approach.¹⁷ The accuracy of T_1 for DESPOT-1 depends on the configuration of the FAs. In this study, the T_1 was calculated by solving the regression problem with a signal acquired using 2 FAs. For the accurate measurement of T_1 , the dynamic range (DR) of the regression line shown in Equation 8 needs to be large. Otherwise, the quantitative value becomes sensitive to the noise or signal artifacts. The DR for a particular TR and T_1 can be expressed as

$$DR(TR, T_1, \theta_1, \theta_2) = \frac{S_{\theta_2}(TR, T_1)}{M_0 \sin(\theta_2)} - \frac{S_{\theta_1}(TR, T_1)}{M_0 \sin(\theta_1)}, \quad (13)$$

where θ_1 and θ_2 are the FAs used for the acquisition, and S_{θ_1} and S_{θ_2} are the SPGR signals with the FAs of θ_1 and θ_2 , respectively. In addition to the DR, the fractional signal (FS) to the SPGR signal with Ernst angle is also related to measurement accuracy. The FS was calculated using the following equation:

$$FS(TR, T_1, \theta_1, \theta_2) = \frac{(S_{\theta_1}(TR, T_1) + S_{\theta_2}(TR, T_1))}{2S_{\theta_E}}, \quad (14)$$

where S_{θ_E} is the SPGR signal with the Ernst angle, derived by $\theta_E = \arccos(e^{-\frac{TR}{T_1}})$. In this study, DR and FS values were calculated for T_1 values between 100 and 1500 ms. The TR of the equation was fixed to 5.8 ms, which was used for the volunteer study. A θ_1 of 3° was used to obtain the proton

density-weighted images for the PDFF measurement. Then, the quasi-optimal angle θ'_2 for θ_2 can be determined by maximizing the production of DR and FS within the T_1 range. Because $FS \times DR$ depends on TR, T_1 , θ_1 and θ_2 , it is complicated to obtain θ'_2 . Therefore, for simplicity of calculation, θ'_2 was determined by solving the following minimization problem:

$$\theta'_2 = \underset{\theta_2 \in \{1, 60\}}{\operatorname{argmax}} \sum_{T_1=100}^{1500} (DR \times FS)_{TR=5.8 \text{ ms}, \theta_1=3^\circ} \quad (15)$$

3.3 | Reconstruction

In this study, the reconstruction was implemented sequentially in the following order: CS, CSE-MRI, and DESPOT-1. At first, the set of MR images was reconstructed using the CS algorithm. The PDFF, R_2^* maps, and water images were calculated using the CSE-MRI-based approach. Finally, T_1 mapping was achieved using DESPOT-1 with the separated water images.

The CS algorithm was implemented offline in MATLAB (MathWorks, Natick, MA). The TV operator used for the L1 regularization was applied to every 6 volumes of the multi-echo MR images. Each volume of the MR images was normalized by their maximum value. The spatial phase variation of the MR images was corrected using the low-resolution images, because the TV is sensitive to the phase variation. The regularization coefficient λ of 0.001 was used. Equation 10 was solved iteratively using the unconstrained split Bregman method,²² which transforms the equation to the L2 and L1 components. The L2 norm component, which is a differential problem, was solved by using the preconditioned conjugate gradients method. The L1 norm problems were solved using the thresholding algorithm (threshold value = 0.002).

The water-fat separation was performed based on the CSE-MRI approach with the multipeak model (420, 318, -94 Hz) proposed by Yu et al.¹⁸ The relative amplitudes of the peaks α in Equation 3 were determined by a self-calibration method using the T_2^* -IDEAL algorithm.¹⁸ The PDFF and R_2^* maps were calculated using the MR images acquired with the FA of 3° to remove T_1 bias, which is the bias caused by T_1 difference of water and fat. The T_1 map was calculated with the DESPOT-1 using the separated water images with FAs of 3° and 19° . Moreover, it is possible to calculate the T_1 map of fat in a same time, if the fat has sufficient signal intensities. However, we only showed the T_1 of water in this paper. To demonstrate the significance of bias to T_1 measurement caused by the presence of fat in a voxel, the T_1 map without water-fat separation was calculated using the DESPOT-1. The calculation was performed using the acquired in-phase MR images (TE = 2.3 ms).

3.4 | Phantom and volunteer studies

Phantom and volunteer studies were implemented on the 3T MRI with whole-body coil and 32-channel torso array for transmitting and receiver RF coil, respectively. To validate the quantitative maps measured with the VFA method, we also performed a multi-TR/TE single-voxel stimulated echo acquisition mode²³ (multi-TR/TE STEAM) and a CSE-MRI-based clinical sequence (IDEAL-IQ, GE Healthcare, Waukesha, WI). The data of the multi-TR/TE STEAM sequence were analyzed with homemade software to measure the T_1 of water and a PDFF. In addition, R_2^* and PDFF maps by IDEAL-IQ were reconstructed on the host computer of the scanner.

In phantom studies, we used hand-made phantoms created according to the following parameters: The phantom was constructed using 10 acrylic containers (inner diameter = 30 mm, outer diameter = 40, height = 35 mm) filled with agarose gel doped with gadolinium at a concentration of 0.0 to 2.0 mM. Peanut oil was mixed with a content ratio of 0, 10, 20, or 100%

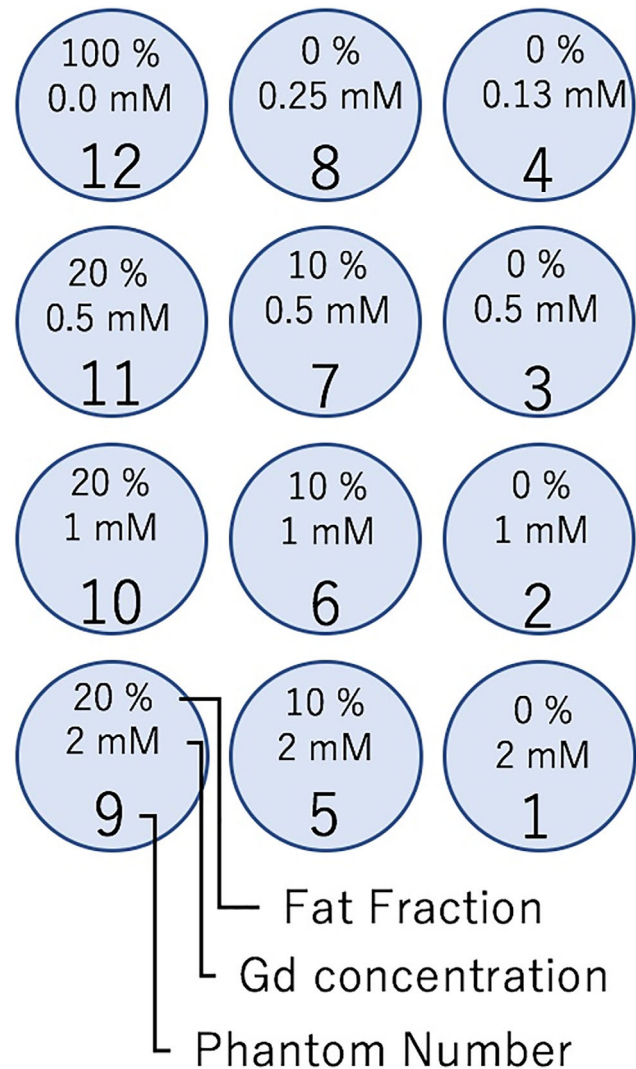


FIGURE 3 Structure and composition of the phantom used in this study. The phantom consists of peanuts oil, gadolinium (Gd), and agarose

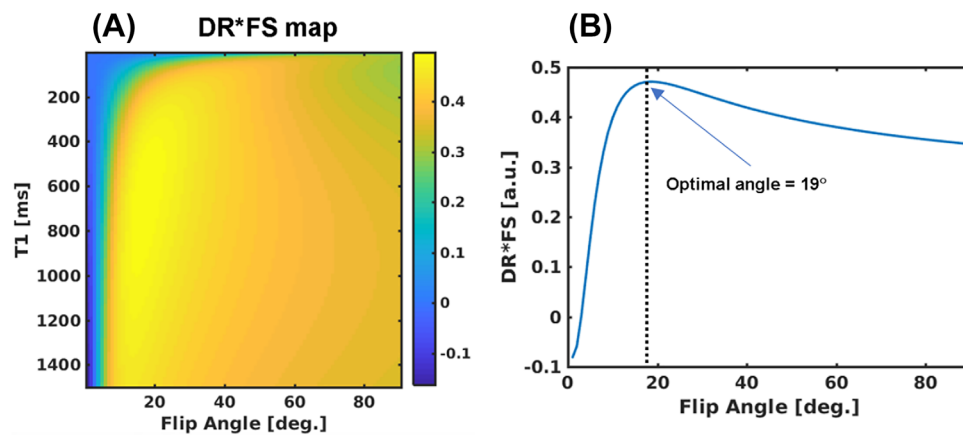


FIGURE 4 A, Dependency of $DR \times FS$ on T_1 and FA. B, Mean value of $DR \times FS$ for the T_1 values. The FA that has a maximum value of $DR \times FS$ is the optimal FA for the T_1 mapping within the range of $T_1 = 100$ to 1500 ms. DR, dynamic range; FS, fractional signal

to adjust the PDF of the phantom. The structure and composition of the phantom are illustrated in Figure 3. Chemical shift frequencies (420, 318, and -94 Hz) of the peanut oil at 3 T have been reported in a previous article.¹⁸ A VFA multi-echo SPGR sequence was performed with the following MR parameters: $TR/TE/\Delta TE = 6.7/1.0/0.9$ ms, $FA = 3^\circ$ and 19° , $FOV = 35$ cm², matrix = $160 \times 160 \times 24$, slice thickness = 4.0 mm). Six echoes ($TE = 1.1, 1.9, 2.7, 3.5, 4.3$, and 5.2 ms) were acquired in every 2 shots to perform the appropriate water-fat separation. A variable-density trajectory ($R = 4.5$) was used for the CS. The water images, PDF, and R_2^* maps were calculated with the T_2^* -IDEAL algorithm¹⁸ using the set of images acquired with FAs of 3° and 19° . The T_1 map was calculated with DESPOT-1 using the separated water images. As references, multi-TR/TE STEAM (TR varied from 150 to 2000 ms, TE varied from 10 to 110 ms, $FA = 90^\circ$, voxel size = 2 cm³, 32 spectra) and IDEAL-IQ ($TR/TE/\Delta TE = 6.7/1.0/0.9$ ms, $FA = 3^\circ$, $FOV = 35$ cm², matrix = $160 \times 160 \times 24$, slice thickness = 4.0 mm, 6 echoes) were acquired.

For the in vivo study, 18 volunteers were recruited to demonstrate the clinical usefulness of the method. The study was approved by our institution, and written informed consent was obtained from the subjects. As with the phantom studies, the quantitative maps of volunteers were acquired using the VFA SPGR sequence ($TR/TE/\Delta TE = 5.6/0.9/0.67$ ms, $FA = 3^\circ$ and 19° , $FOV = 40$ cm², matrix = $160 \times 160 \times 24$, slice thickness = 10.0 mm, scan time = 18 seconds). The TEs of 0.9, 1.5, 2.2, 2.9, 3.5, and 4.2 ms were used for the multi-echo acquisition. The scan was implemented with a single breath-hold. The multi-TR/TE STEAM with the same MR parameters as the phantom study and the IDEAL-IQ sequences ($TR/TE/\Delta TE = 5.6/0.9/0.67$ ms, $FA = 3^\circ$, $FOV = 40$ cm², matrix = $160 \times 160 \times 24$, slice thickness = 10.0 mm, 6 echoes) were implemented. The scanned voxel for the STEAM sequence was placed at the right lobe of the liver, taking care to fit the whole voxel in the liver and to avoid major vessels.

The 3D regions of interest (ROIs) were placed in the right lobe of the liver to measure PDF, T_2^* , and T_1 by

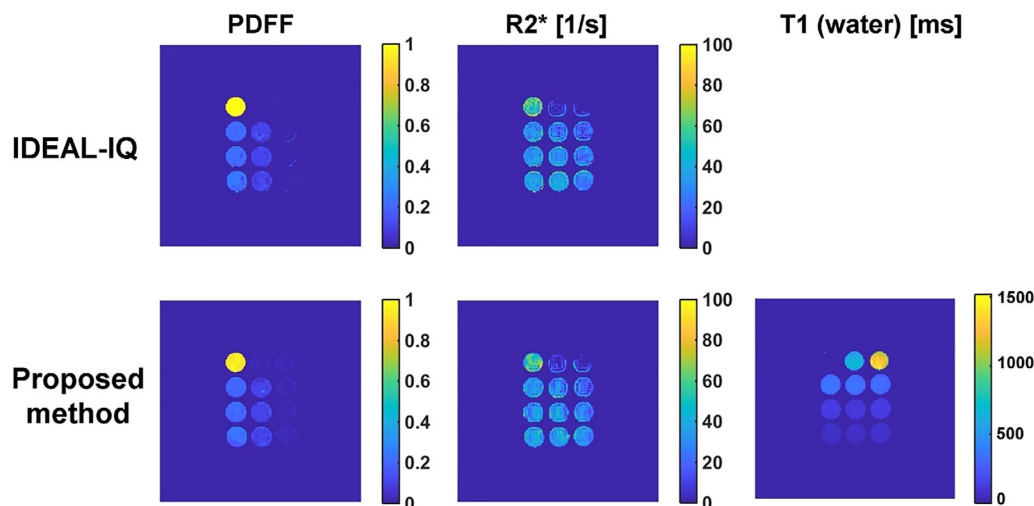


FIGURE 5 Quantitative maps acquired with the IDEAL-IQ and variable flip angle (VFA) method

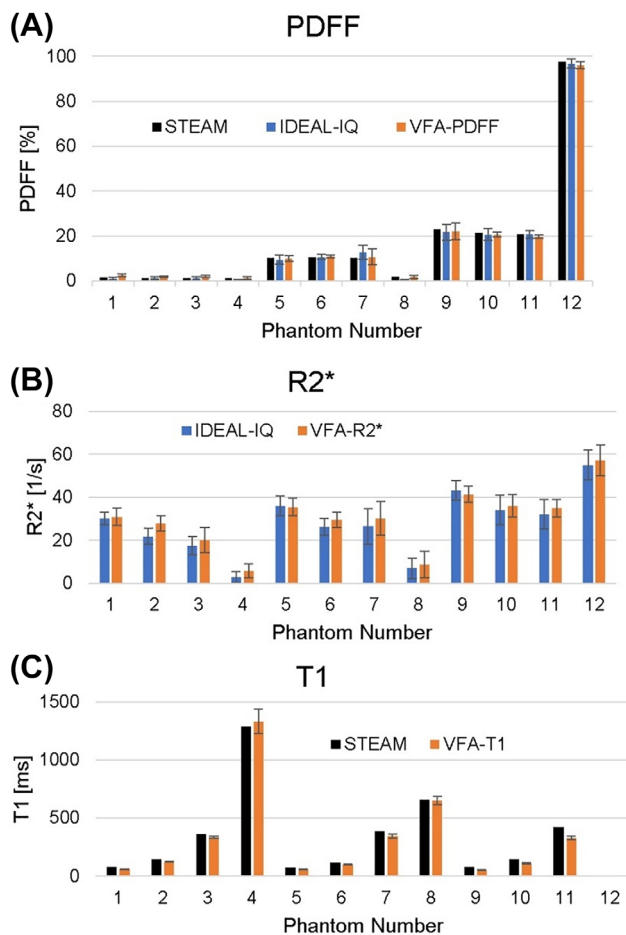


FIGURE 6 Quantitative values of proton density fat fraction (PDFF) (A), R_2^* (B), and T_1 (C) measured with the multi-TR/TE stimulated echo acquisition mode (STEAM), IDEAL-IQ, and VFA methods

quantitative mapping. As a rule, the ROIs were approximately 2.0 cm^3 in size, and the edge of the liver and all major vessels were avoided by referring to the water image.

To test the equivalence of the quantitative values measured with different methods, 2 one-sided paired t-tests were used. The limit of the equivalence intervals for the PDFF, R_2^* , and T_1 were ± 1 percentage point, ± 5 (1/second), and ± 50 ms, respectively. To show the bias to T_1 measurement caused by the presence of fat in the liver, T_1 values were measured using 3 approaches: (1) multi-TR/TE STEAM, (2) DESPOT-1 with in-phase MR images, and (3) DESPOT-1 with separated water images. The t-tests were conducted to compare the T_1 by STEAM and that by DESPOT-1 with in-phase/water image in the subgroups of patients with high PDFF value ($n = 9$, $\text{PDFF} \geq 7$) and low PDFF value ($n = 9$, $\text{PDFF} < 7$) in the liver.

4 | RESULTS

Figure 4A shows how the $\text{DR} \times \text{FS}$ varied with T_1 and FA. This result implies that the optimal FA depends heavily on

the T_1 of the target subject in DESPOT-1. The FA used for this study was determined by assuming that the T_1 values of the liver ranged from 100 to 1500 ms. Figure 4B shows the mean values of $\text{DR} \times \text{FS}$ for the T_1 values. The maximum value was observed at an FA of 19° .

Figure 5 shows the PDFF and R_2^* maps of the phantoms derived using the IDEAL-IQ and VFA method, and also shows the T_1 map as per the VFA method. The values of PDFF, R_2^* , and T_1 as derived by the 3 methods (multi-TR/TE STEAM, IDEAL-IQ, and VFA method) were in close agreement, as shown in Figure 6A-C. The mean values of these phantoms were statistically equivalent ($p < .05$), as given in Table 1. The values and error bars in Figure 6A-C show the mean values and SD inside the ROIs ($\sim 1 \text{ cm}^3$) for each phantom.

Quantitative maps and water images for the volunteer study are shown in Figure 7. The quantitative values ($\text{PDFF} = 11.9 \pm 4.5$ [%], $R_2^* = 45.9 \pm 10.3$ [1/s], $T_1 = 1163 \pm 212$ [ms]) of PDFF, R_2^* , and T_1 in the right lobe were in close agreement with those measured with the IDEAL-IQ

TABLE 1 Correlation coefficient and results of an equivalence test of the quantitative values as derived by the alternative and VFA method

(a) PDFF		
	STEAM v.s. VFA-PDFF	IDEAL-IQ v.s. VFA-PDFF
R^2	0.999	0.988
Mean difference [95 % CI]	0.175 [-0.26, 0.61]	-0.24 [-0.82, 0.34]
P value	0.003	0.02
(b) R_2^*		
		IDEAL-IQ v.s. VFA- R_2^*
R^2		0.9816
Mean difference [95 % CI]		-2.16 [-3.2, -1.1]
P value		0.04
(c) T_1		
		STEAM v.s. VFA- T_1
R^2		0.995
Mean difference [95 % CI]		-2.16 [-3.2, -1.1]
P value		0.012

Note: Statistical tests were applied to show equivalence between the quantitative values of these methods. $p < .05$ indicates that the quantitative values are equivalent within a limit. The limit was set as 1 percentage point for PDFF, 5 (1/second) for R_2^* , and 50 ms for T_1 . CI, confidence interval

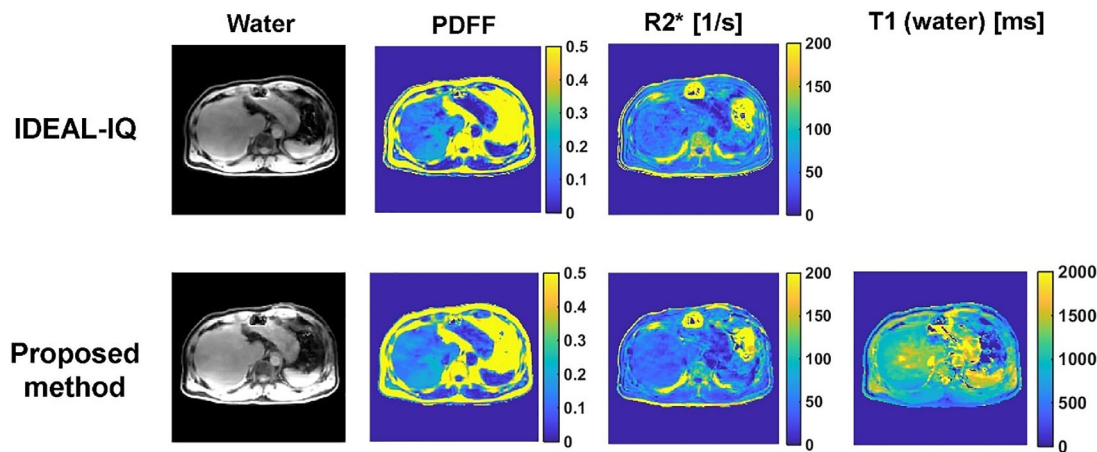


FIGURE 7 Quantitative maps of a volunteer's liver acquired with the IDEAL-IQ and VFA method. The T_1 value (1163 ± 212 ms) of the right lobe was in close agreement with the STEAM result (1170 ms)

(PDFF = 11.0 ± 3.6 [%], $R_2^* = 43.5 \pm 8.7$ [1/s]) and STEAM (PDFF = 10.3 [%], $T_1 = 1170$ [ms]). Figure 8 shows the box plots of T_1 measurements for the subgroups of high PDFF and low PDFF in the liver. The T_1 value measured by DESPOT-1 with in-phase MR images was significantly lower than that measured using multi-TR/TE STEAM only in the subgroup of high PDFF ($p = .024$). This result indicated that the T_1 measurement by in-phase MR images was biased as a result of the presence of fat in a voxel.

5 | DISCUSSION

In this study, we proposed a multiparameter mapping including T_1 , PDFF, and R_2^* using multi-echo spoiled gradient-

echo sequence with variable flip. Phantom studies demonstrated that the PDFF and T_1 acquired with the VFA method were in close agreement with those acquired with conventional methods (IDEAL-IQ) and standard of reference (STEAM), although slight blurring and artifacts, caused by undersampling, were observed. Quantitative maps generated using the VFA method with the multicontrast CS approach were of acceptable quality, even with a high reduction factor of 4.5 to implement the VFA sequence with a single breath-hold. In the last few years, several articles have been devoted to the study of CS for multicontrast or multiphase images. Huang et al proposed a CS with joint total variation, which used the underlying structures of the MR images, for the multi-echo images.²⁴ A reconstruction using a CS in the frequency domain was also proposed for multiphase imaging.²⁵

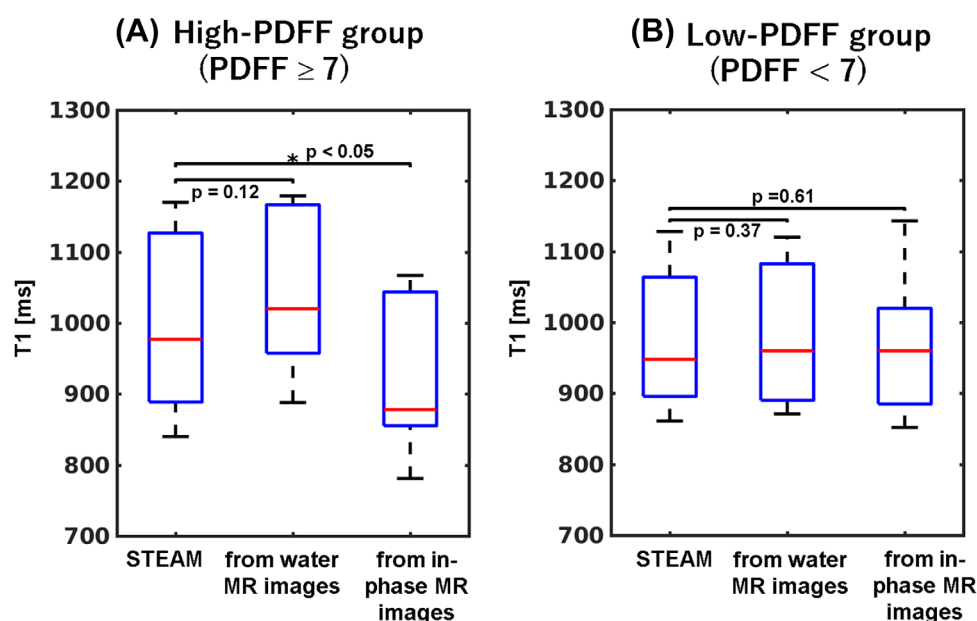


FIGURE 8 Box plots show T_1 measured using multi-TR/TE STEAM, DESPOT-1 with in-phase MR images (without fat-water separation), and DESPOT-1 with separated water images for high-PDFF (A) and low-PDFF (B) groups

Although a small signal loss was observed in their methods, a high reduction factor was achieved in their method. In our study, a CS with total variation was applied in the Fourier domain along the TE dimension, which may affect the quantitative results. However, even with our methods with CS in the TE dimension, the quantitative values including PDFF and R_2^* were no different from those by the method without CS (IDEAL-IQ). This is most likely the result of using a small value of the regularization coefficient so that the quantitative results would not change so much.

To achieve further acceleration of the scan, improving the reconstruction algorithm or parameters is required. In our study, the reconstruction was performed by combining the parallel imaging and CS directly, like sparse-SENSE.²⁶ We used a final acceleration factor of 4.5 to achieve whole-liver coverage. However, we do not think that we maximized the ability of CS. There are some parameters to be optimized to obtain the maximum benefit from the CS approach, including trajectories, regularization coefficients, and sensitivity maps. In this study, the trajectory pattern and coefficient values were manually determined by several trials and errors to obtain better mapping results. Moreover, the sensitivity map was derived using the ESPRiT approach. It might be possible to achieve higher acceleration, to shorten the acquisition time or extend scan coverage, if we optimize these parameters in a future work.

The accuracy of T_1 mapping using DESPOT-1 depends on the FAs and the SPGR signal curves. In this study, we assumed that the range of T_1 in the liver was 100 to 1500 ms. In this range of T_1 , accurate T_1 measurement was achieved with FAs of 3° and 19° . We believe that VFA- T_1 is acceptable for the purpose of evaluating liver disease and function. However, our results would not be applicable for the tissues/organs with a T_1 of greater than 1500 ms, because their appropriate FAs should be different. Another limitation in the T_1 mapping was the B_1^+ inhomogeneity, which could cause a mapping error in the case of higher-field MRI. To solve this problem, combination of T_1 mapping and B_1 mapping is a promising approach,^{27,28} although additional scans or pulses are required. Deoni et al proposed a T_1 and B_1 mapping method (DESPOT-HIFI) using SPGR with an inversion recovery pulse.²⁷ In addition, Reto et al proposed a T_1 mapping method with B_1 inhomogeneity correction acquired with additional measurement.²⁸

There are 2 major limitations in our approach: T_1 bias to PDFF as a result of nonzero FA, and bias to T_1 of water as a result of iron accumulation. This study was intended to develop an additional T_1 mapping to the conventional PDFF and R_2^* mapping. Therefore, in our method and in conventional CSE-MRI-based PDFF measurements, small FAs were used to minimize the T_1 bias to PDFF. However, the small FA approach still has a small amount of T_1 bias and has low SNR. Wang et al proposed a PDFF measurement approach

to correct the T_1 bias using the dual-TR sequence,²⁹ and showed that true PDFF values (or T_1 -corrected PDFF) may be estimated based on SPGR signal equations—including PDFF, off-resonance, T_1 , TE, and TR. This method enables us to use 2 TRs with a higher FA to calculate PDFF, which could also offer SNR benefit. In our study, a bias to T_1 measurement caused by iron accumulation in the liver was not addressed.

In general, liver is an organ that accumulates iron. Several studies have reported a strong association between R_2^* and biopsy-proven hepatic iron concentration.^{30–32} The regression analysis methods proposed in these studies facilitate robust and reproducible quantification of hepatic iron concentration. Accumulated iron in the liver also affects T_1 (shortening T_1). When applying the T_1 measurement to liver fibrosis staging and/or estimation of liver functional, a native T_1 without an effect of iron should be measured. T_1 shortening induced by iron overload is still not clearly understood, although several theories have been proposed to elucidate proton physics in the presence of iron.³³ It is revealed that T_1 has a linear relationship with hepatic iron concentration.^{10,15} Banerjee et al further formulated an iron-corrected T_1 estimation method using the R_2 or R_2^* in an iron-rich liver environment. They also proved that the iron-corrected T_1 was strongly correlated with the Ishak fibrosis stage. It might be better to adopt their approach to our method to measure T_1 of the liver more accurately in a single breath-hold.

6 | CONCLUSION

In this study, we developed a new quantification method to obtain 3D T_1 , R_2^* , and PDFF maps with a single breath-hold. The acquisition was accelerated using a multicontrast CS with total variation. Phantom and volunteer studies demonstrated the accuracy of our method. Our method facilitates noninvasive evaluation of liver fibrosis and function with acceptable accuracy of quantification.

CONFLICT OF INTEREST

Tetsuya Wakayama is an employee of GE Healthcare.

REFERENCES

- [1] Bravo AA, Sheth SG, Chopra S. Liver biopsy. *N Engl J Med*. 2001;344:495-500.
- [2] Ratzliff V, Charlotte F, Heurtier A, et al. Sampling variability of liver biopsy in nonalcoholic fatty liver disease. *Gastroenterology*. 2005;128:1898-1906.
- [3] Poynard T, Lenaour G, Vaillant JC, et al. Liver biopsy analysis has a low level of performance for diagnosis of intermediate stages of fibrosis. *Clin Gastroenterol Hepatol*. 2012;10:657-663.

- [4] Annet L, Peeters F, Abarca-Quinones J, Leclercq I, Moulin P, Van Beers BE. Assessment of diffusion-weighted MR imaging in liver fibrosis. *J Magn Reson Imaging*. 2007;25:122-128.
- [5] Muthupillai R, Lomas DJ, Rossman PJ, Greenleaf JF, Manduca A, Ehman RL. Magnetic resonance elastography by direct visualization of propagating acoustic strain waves. *Science*. 1995; 269:1854-1857.
- [6] Ichikawa S, Motosugi U, Ichikawa T, et al. Magnetic resonance elastography for staging liver fibrosis in chronic hepatitis C. *Magn Reson Med Sci*. 2012;11:291-297.
- [7] Taouli B, Ehman RL, Reeder SB. Advanced MRI methods for assessment of chronic liver disease. *Am J Roentgenol*. 2009;193:14-27.
- [8] Katsube T, Okada M, Kumano S, et al. Estimation of liver function using T1 mapping on Gd-EOB-DTPA-enhanced magnetic resonance imaging. *Invest Radiol*. 2011;46:277-283.
- [9] Haimerl M, Verloh N, Zeman F, et al. Assessment of clinical signs of liver cirrhosis using T1 mapping on Gd-EOB-DTPA-enhanced 3T MRI. *PLoS One*. 2013;8:e85658.
- [10] Banerjee R, Pavlides M, Tunnicliffe EM, et al. Multiparametric magnetic resonance for the non-invasive diagnosis of liver disease. *J Hepatol*. 2014;60:69-77.
- [11] Heye T, Yang S-R, Bock M, et al. MR relaxometry of the liver: significant elevation of T1 relaxation time in patients with liver cirrhosis. *Eur Radiol*. 2012;22:1224-1232.
- [12] Mozes FE, Tunnicliffe EM, Pavlides M, Robson MD. Influence of fat on liver T1 measurements using modified Look-Locker inversion recovery (MOLLI) methods at 3T. *J Magn Reson Imaging*. 2016;44:105-111.
- [13] Hoad CL, Palaniyappan N, Kaye P, et al. A study of T₁ relaxation time as a measure of liver fibrosis and the influence of confounding histological factors. *NMR Biomed*. 2015;28:706-714.
- [14] Liu C-Y, McKenzie CA, Yu H, Brittain JH, Reeder SB. Fat quantification with IDEAL gradient echo imaging: correction of bias from T1 and noise. *Magn Reson Med*. 2007;58:354-364.
- [15] Elizabet T, Robson M, Banerjee R. Medical imaging. Patent UK 1304728.7, 201.
- [16] Reeder SB, Wen Z, Yu H, et al. Multicoil Dixon chemical species separation with an iterative least-squares estimation method. *Magn Reson Med*. 2004;51:35-45.
- [17] Deoni SCL, Rutt BK, Peters TM. Rapid combined T1 and T2 mapping using gradient recalled acquisition in the steady state. *Magn Reson Med*. 2003;49:515-526.
- [18] Yu H, Shimakawa A, McKenzie CA, Brodsky E, Brittain JH, Reeder SB. Multiecho water-fat separation and simultaneous R2* estimation with multifrequency fat spectrum modeling. *Magn Reson Med*. 2008;60:1122-1134.
- [19] Lustig M, Donoho D, Pauly JM. Sparse MRI: the application of compressed sensing for rapid MR imaging. *Magn Reson Med*. 2007;58:1182-1195.
- [20] Lustig M, Donoho DL, Santos JM, Pauly JM. Compressed sensing MRI. *IEEE Signal Process Mag*. 2008;25:72-82.
- [21] Uecker M, Lai P, Murphy MJ, et al. ESPIRiT—an eigenvalue approach to autocalibrating parallel MRI: where SENSE meets GRAPPA. *Magn Reson Med*. 2014;71:990-1001.
- [22] Goldstein T, Osher S. The split Bergman method for L1-regularized problems. *SIAM J Imaging Sci*. 2009;2:323-343.
- [23] Hamilton G, Middleton MS, Hooker JC, et al. In vivo breath-hold (1) H MRS simultaneous estimation of liver proton density fat fraction, and T1 and T2 of water and fat, with a multi-TR, multi-TE sequence. *J Magn Reson Imaging*. 2015;42:1538-1543.
- [24] Huang J, Chen C, Axel L. Fast multi-contrast MRI reconstruction. *Magn Reson Imaging*. 2014;32:1344-1352.
- [25] Otazo R, Kim D, Axel L, Sodickson DK. Combination of compressed sensing and parallel imaging for highly accelerated first-pass cardiac perfusion MRI. *Magn Reson Med*. 2010;64:767-776.
- [26] Liang D, Liu B, Wang J, Ying L. Accelerating SENSE using compressed sensing. *Magn Reson Med*. 2009;62:1574-1584.
- [27] Deoni SC. High-resolution T1 mapping of the brain at 3T with driven equilibrium single pulse observation of T1 with high-speed incorporation of RF field inhomogeneities (DESPOT1-HIFI). *J Magn Reson Imaging*. 2007;26:1106-1111.
- [28] Treier R, Steingoetter A, Fried M, Schwizer W, Boesiger P. Optimized and combined T1 and B1 mapping technique for fast and accurate T1 quantification in contrast-enhanced abdominal MRI. *Magn Reson Med*. 2007;57:568-576.
- [29] Wang X, Hernando D, Wines C, Reeder SB. In: Proceedings of the 25th Annual Meeting of ISMRM, Honolulu, HI, 2017. p. 3961.
- [30] Wood JC, Enriquez C, Ghugre N, et al. MRI R2 and R2* mapping accurately estimates hepatic iron concentration in transfusion-dependent thalassemia and sickle cell disease patients. *Blood*. 2005;106:1460-1465.
- [31] Hankins JS, McCarville MB, Loeffler RB, et al. R2* magnetic resonance imaging of the liver in patients with iron overload. *Blood*. 2009;113:4853-4855.
- [32] Henninger B, Kremser C, Rauch S, et al. Evaluation of MR imaging with T1 and T2* mapping for the determination of hepatic iron overload. *Eur Radiol*. 2012;22:2478-2486.
- [33] Ghugre NR, Coates TD, Nelson MD, Wood JC. Mechanisms of tissue-iron relaxivity: nuclear magnetic resonance studies of human liver biopsy specimens. *Magn Reson Med*. 2005;54:1185-1193.

How to cite this article: Tamada D, Wakayama T, Onishi H, Motosugi U. Multiparameter estimation using multi-echo spoiled gradient echo with variable flip angles and multicontrast compressed sensing. *Magn Reson Med*. 2018;80:1546–1555. <https://doi.org/10.1002/mrm.27151>